



Universiteit
Leiden
The Netherlands

The Green Bank Ammonia Survey: Unveiling the Dynamics of the Barnard 59 Star-forming Clump

Redaelli, E.; Alves, F.O.; Caselli, P.; Pineda, J.E.; Friesen, R.K.; Chacón-Tanarro, A.; ... ; Seo, Y.M.

Citation

Redaelli, E., Alves, F. O., Caselli, P., Pineda, J. E., Friesen, R. K., Chacón-Tanarro, A., ... Seo, Y. M. (2017). The Green Bank Ammonia Survey: Unveiling the Dynamics of the Barnard 59 Star-forming Clump. *Astrophysical Journal (Issn 0004-637X)*, 850, 202.
doi:10.3847/1538-4357/aa9703

Version: Not Applicable (or Unknown)

License: [Leiden University Non-exclusive license](#)

Downloaded from: <https://hdl.handle.net/1887/58717>

Note: To cite this publication please use the final published version (if applicable).



The Green Bank Ammonia Survey: Unveiling the Dynamics of the Barnard 59 Star-forming Clump

E. Redaelli¹, F. O. Alves¹, P. Caselli¹, J. E. Pineda¹, R. K. Friesen²,
A. Chacón-Tanarro¹, C. D. Matzner³, A. Ginsburg⁴, E. Rosolowsky⁵, J. Keown⁶, S. S. R. Offner⁷, J. Di Francesco^{6,8},
H. Kirk⁸, P. C. Myers⁹, A. Hacar^{10,11}, A. Cimatti¹², H. H. Chen¹³, M. C. Chen⁶, K. I. Lee¹³, and Y. M. Seo¹⁴

¹ Max Planck Institut für Extraterrestrische Physik, Giessenbachstrasse 1, D-85748, Garching, Germany; eredaelli@mpe.mpg.de
² Dunlap Institute for Astronomy and Astrophysics, University of Toronto, 50 St. George Street, Toronto, ON, M5S 3H4, Canada

³ Department of Astronomy & Astrophysics, University of Toronto, 50 St. George Street, Toronto, Ontario, M5S 3H4, Canada

⁴ National Radio Astronomy Observatory, Socorro, NM 87801, USA

⁵ Department of Physics, University of Alberta, Edmonton, AB, Canada

⁶ Department of Physics and Astronomy, University of Victoria, Victoria, BC, V8P 5C2, Canada

⁷ Department of Astronomy, University of Massachusetts, Amherst, MA 01003, USA

⁸ NRC Herzberg Astronomy and Astrophysics, 5071 West Saanich Road, Victoria, BC, V9E 2E7, Canada

⁹ Harvard-Smithsonian Center for Astrophysics, 60 Garden Street, Cambridge, MA 02138, USA

¹⁰ Leiden Observatory, Leiden University, P.O. Box 9513, 2300-RA Leiden, The Netherlands

¹¹ Institute for Astrophysics, University of Vienna, Trkenschanzstrasse 17, A-1180 Vienna, Austria

¹² Dipartimento di Fisica e Astronomia, Università di Bologna, Via Piero Gobetti 93/2, I-40129 Bologna, Italy

¹³ Harvard-Smithsonian Center for Astrophysics, Cambridge, MA 02138, USA

¹⁴ Jet Propulsion Laboratory, NASA, 4800 Oak Grove Dr., Pasadena, CA 91109, USA

Received 2017 August 21; revised 2017 October 16; accepted 2017 October 26; published 2017 December 4

Abstract

Understanding the early stages of star formation is a research field of ongoing development, both theoretically and observationally. In this context, molecular data have been continuously providing observational constraints on the gas dynamics at different excitation conditions and depths in the sources. We have investigated the Barnard 59 core, the only active site of star formation in the Pipe Nebula, to achieve a comprehensive view of the kinematic properties of the source. This information was derived by simultaneously fitting ammonia inversion transition lines (1, 1) and (2, 2). Our analysis unveils the imprint of protostellar feedback, such as increasing line widths, temperature, and turbulent motions in our molecular data. Combined with complementary observations of dust thermal emission, we estimate that the core is gravitationally bound following a virial analysis. If the core is not contracting, another source of internal pressure, most likely the magnetic field, is supporting it against gravitational collapse and limits its star formation efficiency.

Key words: ISM: individual objects (Barnard 59) – ISM: kinematics and dynamics – ISM: molecules – ISM: structure – radio lines: ISM – stars: formation

1. Introduction

Low-mass star formation occurs through the fragmentation of molecular clouds into smaller and colder dense cores, where protostars can possibly form (Andre et al. 2000). The efficiency for the whole process is low (e.g., usually less than 10% of the cloud mass is converted into stars, see Evans et al. 2009) due to multiple reasons: cores can be transient objects because, for instance, they are not massive enough to collapse, or the feedback from the first protostars can disperse the gas before it can form new stars. Planck polarimetric observations (Planck Collaboration et al. 2016) have revealed that molecular clouds are often magnetized, and that the magnetic fields that thread their filamentary structure (André et al. 2010) are usually aligned perpendicular to the filaments' long axes, especially at higher column density (see, for instance, Palmeirim et al. 2013 for the Taurus molecular cloud). In this configuration, magnetic fields can regulate the contraction of the structures more efficiently than interstellar turbulence, depending on the level of turbulence with respect to the magnetic field (e.g., Nakamura & Li 2008; Seifried & Walch 2015). To better constrain the theoretical models, detailed observations of recent star-forming regions are needed. In particular, molecular data of rotational transitions, from which the source density, temperature, velocity, and other

parameters can be inferred, can help enlighten many aspects of the star formation that still lack a complete explanation, such as the effects of feedback from young sources on the parental cloud or the role of the magnetic field.

The Pipe Nebula, a filamentary molecular cloud located at ≈ 145 pc (Alves & Franco 2007), represents an ideal environment to study the early stages of star formation. The cloud is known to exhibit a very low star formation efficiency ($\approx 0.06\%$, Forbrich et al. 2009). Despite its reservoir of cold gas ($M_{\text{tot}} \approx 10^4 M_{\odot}$, Onishi et al. 1999; Lombardi et al. 2006), only its extreme northwest end (Barnard 59, hereafter B59) shows signs of recent star-forming activity, as indicated by the detection of several young stellar objects (YSOs) by the *Spitzer* Cores to Disks (c2d) survey (Brooke et al. 2007). Furthermore, some of these YSOs are driving outflows, which inject enough energy in the cloud to sustain the turbulence level of the gas at sub-parsec scales and to slow down the gravitational collapse (Duarte-Cabral et al. 2012). This hypothesis is consistent with the monolithic dust distribution profile reported by Román-Zúñiga et al. (2012), which implies a lack of further fragmentation. It is not clear why B59 is the only active region in a cloud with numerous prestellar cores (total of 159, Lada et al. 2008). The answer can possibly be found in the morphology of the magnetic field, which is less uniform around B59 in comparison with the

rest of the cloud (Franco et al. 2010). These authors suggest that the locally disorganized field may have allowed the core to form by turbulent compression. Moreover, Peretto et al. (2012) suggested that a large-scale external compression, possibly due to stellar winds from the close Sco OB2 association, may have shaped the filamentary structure of the cloud, and it is interesting to notice that this association is closer to the western part of the Pipe, where B59 is located. A deeper analysis of the kinematics of B59 will help us understand the star-forming process at core scales, and also determine its feedback on the parental cloud.

Ammonia (NH_3) emission has been an important tool for studying the coldest phases of the interstellar medium (Benson & Myers 1989). Its rotational states with $J = K$ are split into doublets due to the ability of the nitrogen atom to tunnel quantum-mechanically through the plane of H atoms, giving rise to the so-called inversion transitions (Ho & Townes 1983), labeled as (J, J) . They are characterized by a critical density $n_{\text{cr}}^{15} \approx 10^{3-4} \text{ cm}^{-3}$ (Shirley 2015). In addition, the fact that ammonia does not appear to freeze-out significantly onto dust grains even at very low temperatures (e.g., Tafalla et al. 2002) makes NH_3 one of the best probes for dense ($n \gtrsim 10^4 \text{ cm}^{-3}$) and cold ($T \lesssim 10 \text{ K}$) environments. Spectral fitting of several ammonia inversion transitions therefore can provide crucial information about the source properties, such as its kinematic structure, density, and temperature.

We used ammonia (1, 1) and (2, 2) data to investigate the kinematics of Barnard 59 and to analyze the protostellar feedback on the core (in Section 4). In Section 5, we combined the NH_3 -derived information with dust thermal emission data at far-infrared wavelengths, to compare the gas and the dust properties. We also performed a simple virial analysis, illustrated in Section 6, to investigate the core dynamical state.

2. Observations

The NH_3 (1, 1) and (2, 2) inversion transitions in B59 were observed between 2015 and 2016 with the Green Bank Telescope (GBT) as part of a Large Program, the Green Bank Ammonia Survey (GAS—Friesen et al. 2017), whose aim is to study dense gas in several molecular clouds in the Gould Belt using ammonia and other molecular tracers. The GAS project used the K-band Focal Plane Array (KFPA) receiver combined with the VErsatile GBT Astronomical Spectrometer backend in configuration Mode 20, which provides eight spectral windows for each of the seven KFPA beams with 23.44 MHz bandwidth and 4096 channels, corresponding to a spectral resolution of 5.72 KHz ($\approx 0.07 \text{ km s}^{-1}$ at $\nu = 23 \text{ GHz}$). Two spectral windows are centered at the ammonia (1, 1) and (2, 2) rest frequencies, which are, respectively, $\nu_{11} = 23694.4955 \text{ MHz}$ and $\nu_{22} = 23722.6336 \text{ MHz}$. More lines were observed, and will be presented in future papers. The chosen setup allows for an in-band frequency switching with a frequency shift of 4.11 MHz. At 23.7 GHz, the KFPA beam size is $\text{FWHM} \approx 31''.8$, which at the distance of 145 pc is equivalent to a spatial resolution of 0.02 pc. The Moon and Jupiter were used as flux calibrators. Since the Moon's angular size is big enough to cover the entire KFPA sky footprint, it was used to determine the relative beam gains. GBTIDL¹⁶ was used to read the raw data into sdfits format and to compute the relative beam gains. The data reduction was performed using Python scripts (available

on GitHub¹⁷), which calls the GBT KFPA pipeline (Masters et al. 2011) for the calibration in main beam temperature (T_{MB}). Then the imaging was performed with custom GAS routines. The maps were acquired in On-The-Fly mode across $10' \times 10'$ tiles. The observations were gridded according to Mangum et al. (2007), using a pixel size of one-third of the beam FWHM at the NH_3 (1, 1) frequency. For further details on the observing setup or on the data reduction, please refer to Friesen et al. (2017). Barnard 59 GAS data belong to the second data release (DR2) of the survey, and thus were not published in Friesen et al. (2017).

2.1. Results

The NH_3 (1, 1) and (2, 2) spectra from the brightest pixel are shown in Figure 1. The rms noise map was determined by taking the intensity standard deviation for each pixel along the spectral axis for all line-free channels. Figure 2 shows histograms of the rms distribution. For both lines, a double peaked distribution is present, with the first maximum at rms $\approx 0.13 \text{ K}$. The second peak at higher values is due to pixels at the map's edges, where the on-source time is lower. If we exclude these noisy edges, the average rms value is $\approx 0.15 \text{ K}$ per channel for both lines. This value is higher than the target level expected by the GAS survey ($\approx 0.10 \text{ K}$), mainly due to the fact that Barnard 59 is mostly at low elevation at the Green Bank latitude (maximum elevation: $\approx 25^\circ$).

2.2. Smoothing and Regridding

The detection of at least two inversion transitions is necessary to determine the kinetic temperature and column density of NH_3 (see Section 3.2 and Appendix A). The NH_3 (2, 2) line in most pixels is undetected, except for a small region in the central part of the dense core (less than 5 arcmin²). To improve the signal-to-noise ratio (S/N) of the observations, we smoothed the cubes to a resolution of $\text{FWHM} = 40''$. The regridded spectral cubes preserve the original number of three pixels per beam. Therefore, the new pixel size was computed following

$$\text{pxl_sz}_{\text{new}} = \frac{\text{FWHM}_{\text{new}}}{3} \approx 13''.33. \quad (1)$$

The regridding was performed using the python FITS_tools¹⁸ package.

2.3. Ancillary Data Sets

We used the dust emission data obtained with *Herschel* to derive the molecular hydrogen column density and the dust temperature in B59 (see Section 5). We used the SPIRE maps of the Pipe Nebula at 250 μm , 350 μm , and 500 μm available in the *Herschel* Science Archive (Observational ID: 1342216013). We have selected the level 3 maps, i.e., the data are already calibrated and the maps are mosaiced. The angular resolutions of those data are approximately 20'' (250 μm), 27'' (350 μm), and 38'' (500 μm).

In addition, we used the LABOCA dust thermal emission map acquired with APEX telescope at 870 μm to compute the total mass of the core. These data have a spatial resolution of 21''.2. They are publicly available in the APEX database.

¹⁵ n_{cr} is computed as the ratio between the Einstein coefficient of spontaneous emission and the sum over the collisional rates.

¹⁶ <http://gbtidl.nrao.edu/>

¹⁷ <https://github.com/GBTAmmoniaSurvey/GAS>

¹⁸ FITS_tools is available at https://github.com/keflavich/FITS_tools.

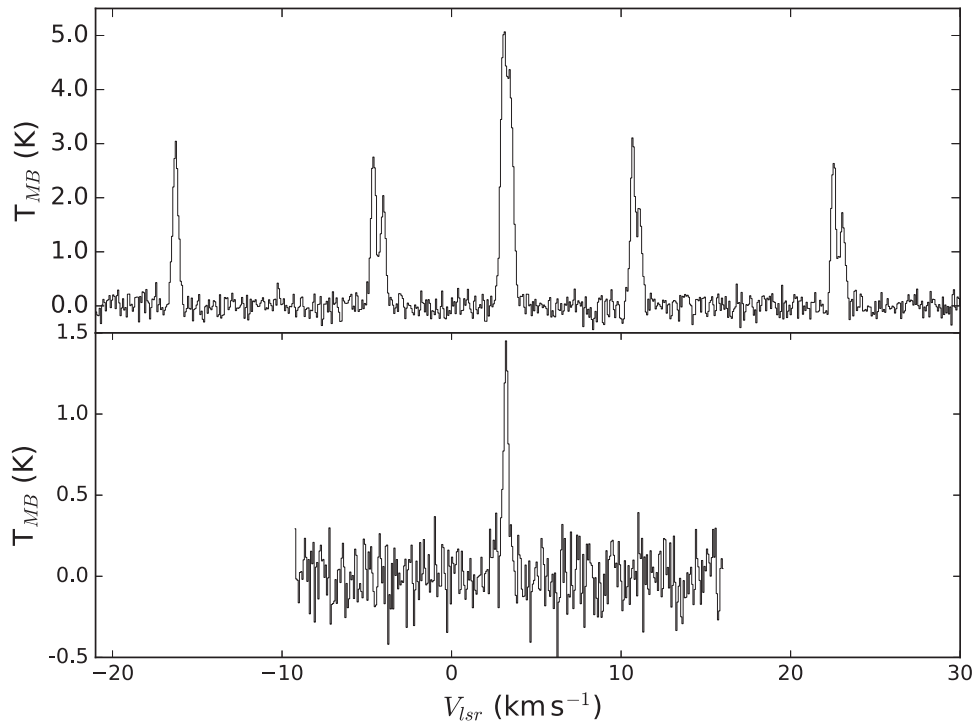


Figure 1. NH_3 (1, 1) (upper panel) and (2, 2) (lower panel) spectra from the brightest pixel (R.A. = $17^{\text{h}}11^{\text{m}}20^{\text{s}}.03$, decl. = $-27^{\circ}26'27''.1$ (J2000)). The hyperfine structure is clearly visible for the (1, 1), while for the (2, 2) only the main group is detectable because the satellite components are too faint.

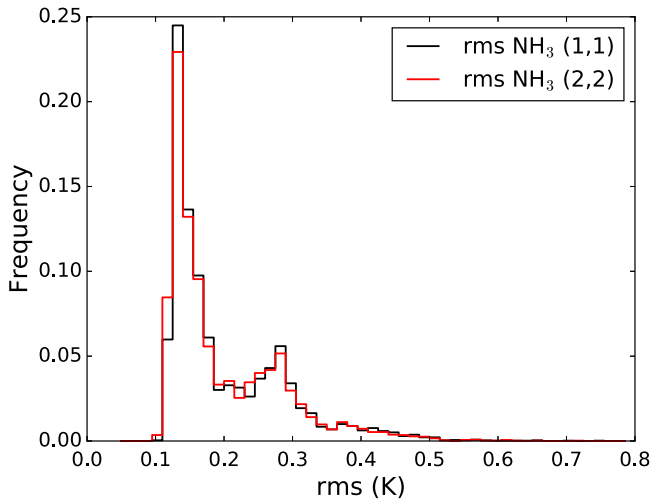


Figure 2. Frequency histogram of rms per channel for the (1, 1) and the (2, 2) lines in black and red, respectively. The data were binned with a spacing of 0.015 K.

3. Data Analysis

3.1. Spectral Fitting Procedure

The NH_3 transitions have been analyzed to derive five line parameters: excitation temperature T_{ex} , kinetic temperature T_K , centroid velocity V_{lsr} , velocity dispersion σ_V , and ammonia total column density $N(\text{NH}_3)$. The theoretical bases for this technique are explained in Appendix A. The spectra were fitted using these variables as free parameters. Our approach consists of a nonlinear gradient descent regression, performed using the Python dedicated library PYSPECKIT¹⁹ (Ginsburg & Mirocha 2011). The implemented code, available on the GAS GitHub

Table 1
Initial Guesses for the Fit

Parameter	Initial Guess	Value Range
$\log[N(\text{NH}_3)/\text{cm}^{-2}]$	14.5	[12.0; 17.0]
T_K (K)	12.0	[5.0; ...]
T_{ex} (K)	8.0	[2.8; ...]
V_{lsr} (km s^{-1})	3.37 ^a	[2.0; 4.0]
σ_V (km s^{-1})	0.11 ^a	[0.04; ...]
OPR	1.0	fixed

Note.

^a V_{lsr} and σ_V values derived from the calculation of moment 1 and moment 2 on the (1, 1) cube.

repository, fits both lines simultaneously pixel by pixel starting from the position with the highest S/N and using their best-fit values as guesses for nearby pixels. Table 1 summarizes the choices made for both initial guesses and parameter ranges, set to prevent unphysical results. The lower limit in velocity dispersion is set to be larger than the spectral resolution ($\text{FWHM} = 0.07 \text{ km s}^{-1}$ corresponds to $\sigma \approx 0.03 \text{ km s}^{-1}$). The centroid velocity range is derived from the values obtained with C^{18}O in Duarte-Cabral et al. (2012). We masked pixels with low S/N based on the rms map and the peak value in the main beam brightness temperature of the NH_3 (1, 1) line (T_{peak}), according to $\text{S/N}_{\text{peak}} = T_{\text{peak}}/\text{rms} > 3.0$. The ortho-to-para ratio (OPR) has been fixed on $\text{OPR} = 1.0$, since we do not have any detection of ortho- NH_3 transitions.²⁰ The uncertainties for each parameter are estimated from the diagonal of the covariance matrix returned by the least-square fitter.

²⁰ Note that this is different in the approach (but not in the results) from the method used in Friesen et al. (2017). There the OPR is set to 0 (no ortho states) and then the derived column density is doubled to obtain the total $N(\text{NH}_3)$.

¹⁹ Available at <https://github.com/pyspeckit/pyspeckit.git>.

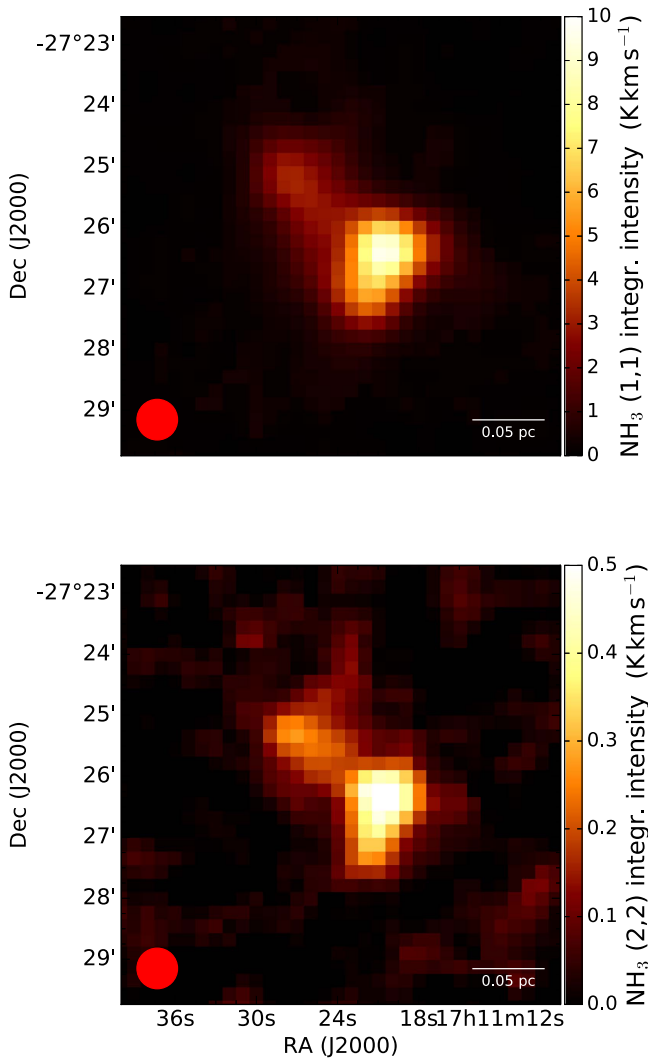


Figure 3. Integrated intensity maps of the NH_3 (1, 1) (upper panel) and (2, 2) (lower panel) lines, obtained with the method described in the text (Section 3.2). The mean rms on-source are 0.06 K km s^{-1} and 0.03 K km s^{-1} , respectively. Here, and in all the following figures, the beam and scale bar are, respectively, shown in the bottom left and right corners.

3.2. Data Masking

The initial threshold imposed on S/N_{peak} is sensitive to the presence of noise spikes in the spectra. Therefore, some pixels still present poorly constrained fitting results. To mask these, we took into account two further parameters: their uncertainties evaluated by the fitting procedure and the S/N in integrated intensity. The latter is calculated using the best-fit spectra previously obtained to select the correct spectral windows for the integration. This approach is better than using a fixed spectral range for the whole map, since it takes into account velocity gradients. We flag channels with signals lower than 0.0125 K , and sum over the remaining ones. For those pixels where no line fit model is available, or at the positions where the fit is poorly constrained (which is evaluated taking into account the uncertainty on velocity dispersion), we adopt a fixed spectral window based on the mean V_{lsr} and σ_V across the source. At each pixel, the integrated intensity uncertainty is calculated through $\epsilon = \text{rms } \Delta V \sqrt{N}$, where ΔV is the channel width and N is the number of channels involved in the

integration. Figure 3 shows the resulting integrated intensity maps for the (1, 1) and (2, 2) transitions.

Table 2 summarizes the criteria adopted to flag the data. Note that for T_{ex} , V_{lsr} , and σ_V , which are derived from the detection of the (1, 1) transition only, we chose a threshold on S/N in (1, 1) integrated intensity. On the other hand, T_K and $N(\text{NH}_3)$ depend on the ratio between the (1, 1) and (2, 2) lines and therefore the additional $S/N_{22} > 3.0$ condition is required. This approach differs from the one used in Friesen et al. (2017) in the sense that we also take into account each of the parameter uncertainties in the masking, and not only the integrated intensity S/N .

3.3. Fitting Results

Figure 4 shows the main component of the NH_3 (1, 1) spectra at different positions across B59, overlaid with the obtained best-fit model. The positions are separated by a smoothed beam size. The overall quality of the fit is good. Across the entire source, we do not see evident signs of the presence of multiple velocity components along the line of sight.

The ammonia column density map, shown in Figure 5, has a denser region in the southwest part of the source, with a peak of $\log[N(\text{NH}_3)]_{\text{peak}} = (14.80 \pm 0.01)$ ²¹ at R.A. = $17^{\text{h}}11^{\text{m}}21^{\text{s}}00$, decl. = $-27^{\circ}26'27''.3$ (J2000). A local increase of the $N(\text{NH}_3)$ is also present toward the NE direction, with a peak of $\log[N(\text{NH}_3)]_{\text{peak}} = (14.27 \pm 0.03)$ at R.A. = $17^{\text{h}}11^{\text{m}}27^{\text{s}}00$, decl. = $-27^{\circ}25'27''.06$ (J2000). Toward the north, a third local maximum is visible, with a peak value of $\log[N(\text{NH}_3)]_{\text{peak}} = (14.26 \pm 0.15)$ at position R.A. = $17^{\text{h}}11^{\text{m}}23^{\text{s}}00$, decl. = $-27^{\circ}24'40''.6$ (J2000). The mean value across the whole source is $\langle \log[N(\text{NH}_3)] \rangle = 14.23$.

Figure 6 shows the kinetic temperature map. The densest part of the cloud is also the coldest: $\langle T_K \rangle = 11.3 \text{ K}$ for regions where $\log[N(\text{NH}_3)] > 14.4$, a typical value for cold cores heated only by the external radiation field and cosmic rays (Evans et al. 2001; Zucconi et al. 2001). In the northern part of the cloud, temperatures are higher, reaching 16–17 K, which possibly indicates another source of heating in addition to the standard cosmic-ray field or surrounding radiation field.

The excitation temperature, which regulates the population levels within each K -ladder, is shown in Figure 7. The data are more spatially extended than the previous two maps due to the flagging criteria on integrated intensity S/N (i.e., the (1, 1) transition has more pixels meeting these criteria than the (2, 2) transition). High column density regions show higher T_{ex} since the upper state becomes more populated through collisions. The mean value across the entire map is $\langle T_{\text{ex}} \rangle = 4.83 \text{ K}$, but it rises to $\langle T_{\text{ex}} \rangle = 5.99 \text{ K}$ at regions where $\log[N(\text{NH}_3)] > 14.4$. The peak value is $T_{\text{ex}}^{\text{peak}} = (7.46 \pm 0.05) \text{ K}$, found at position R.A. = $17^{\text{h}}11^{\text{m}}19^{\text{s}}99$, decl. = $-27^{\circ}26'27''.3$ (J2000), within a beam width from the column density peak. It is interesting to notice that generally T_K is $\approx 7 \text{ K}$ greater T_{ex} , which suggests that the molecule is subthermally excited (i.e., the volume density averaged within the beam is lower than the critical density).

The centroid velocity and velocity dispersion maps are shown in Figures 8 and 9, respectively. V_{lsr} has values in the range $\approx [3.0\text{--}3.8] \text{ km s}^{-1}$, in good agreement with previous

²¹ Throughout the whole paper, column densities are expressed in unity of $\log_{10}[\text{cm}^{-2}]$, unless otherwise stated.

Table 2
Pixels Masking Criteria for the Different Free Parameters

T_K	T_{ex}	$N(\text{NH}_3)$	σ_V	V_{lsr}
$S/N_{22} > 3.0$	$S/N_{11} > 3.0$	$S/N_{22} > 3.0$	$S/N_{11} > 3.0$	$S/N_{11} > 3.0$
$T_K > 5.0 \text{ K}$	$T_{\text{ex}} > 2.8 \text{ K}$	$T_K > 5.0 \text{ K}$	$\epsilon_{\sigma_V} < 0.1 \text{ km s}^{-1}$	$\epsilon_{V_{\text{lsr}}} < 0.1 \text{ km s}^{-1}$
$\epsilon_{T_K} < 3.0 \text{ K}$	$\epsilon_{T_{\text{ex}}} < 3.0 \text{ K}$	$\epsilon_{T_K} < 3.0 \text{ K}$
	...	$T_{\text{ex}} > 2.8 \text{ K}$

observations that report an ambient velocity of 3.6 km s^{-1} (Onishi et al. 1999; Duarte-Cabral et al. 2012). The densest and coldest part of the core shows a kinematically coherent structure, with a mean value $\langle V_{\text{lsr}} \rangle = (3.29 \pm 0.07) \text{ km s}^{-1}$ (computed on pixels with $\log[N(\text{NH}_3)] > 14.4$).

The velocity dispersion range is $\approx [0.05\text{--}0.50] \text{ km s}^{-1}$. The mean value is $\langle \sigma_V \rangle = 0.21 \text{ km s}^{-1}$, and it decreases to $\langle \sigma_V \rangle = 0.18 \text{ km s}^{-1}$ in the densest part of the core.

4. Protostellar Feedback

Brooke et al. 2007 studied the B59 region using *Spitzer* data belonging to the c2d survey, and found approximately 20 YSOs possibly associated with B59. The authors derived each source's spectral class according to the SED slope, following the prescriptions introduced by Lada & Wilking (1984) and developed further by Andre et al. (2000). The latter is defined as $\alpha = d \log(\lambda F_\lambda) / d \log(\lambda)$ between 2.2 and $8.0 \mu\text{m}$. This parameter traces the evolutionary stage of YSOs, since as time passes by the contribution from the central object becomes more important than the dusty envelope emission at larger wavelengths. Hence, the SED slope changes from positive to negative. Class I sources are identified by $\alpha > 0.3$, while Class II sources are represented by $\alpha < -0.3$. Sources with $-0.3 < \alpha < 0.3$ are classified as flat (or I/II). Finally, Class 0 objects present $T_{\text{bol}} < 70 \text{ K}$ and $L_{\text{submm}}/L_{\text{bol}} > 0.5\%$, i.e., a large fraction of their emission is at submillimeter wavelengths.

We refer to Table 2 of Brooke et al. (2007) for the sources' positions, identification names, and spectral classes (after the correction for extinction, when available). To analyze the impact of protostellar feedback from the YSOs into the ambient cloud, we search for a correlation between velocity dispersion and the YSOs positions. As one can see in Figure 9, evolved Class II sources are mostly located at lines of sight of low velocity dispersion. This correspondence suggests that these objects are possibly no longer embedded, being either foreground or background sources. On the other hand, some of the less evolved objects are located in zones of broader lines or at the edge of a transition area. In particular, BHB07-11 (B11, labeled as #11 in the figures), one of the youngest sources in the protocluster (Hara et al. 2013), is found in one of the zones with the highest σ_V values. It is useful to compare these values with the isothermal sound speed, which at $T_K = 11 \text{ K}$, approximately the average kinetic temperature at the high density regions, is

$$C_s = \sqrt{\frac{k_B T_K}{\mu m_H}} = 0.20 \text{ km s}^{-1}, \quad (2)$$

where $\mu = 2.33$ is the mean molecular weight of the gas (which is assumed to be composed mostly by H_2 and a fraction of 10% of He), k_B is the Boltzmann constant, and m_H is the mass of the hydrogen atom. The densest part of B59 is then characterized by marginally subsonic velocity dispersion

($\langle \sigma_V \rangle = 0.18 \text{ km s}^{-1}$, see Section 3.3), and appears to be a quiescent and coherent structure. We will thus refer to it as a coherent core (Goodman et al. 1998).

In order to quantify the amount of turbulence in the source, we separate the thermal σ_{Th} and nonthermal σ_{NT} components of the velocity dispersion (Myers et al. 1991). The former is calculated through

$$\sigma_{\text{Th}} = \sqrt{\frac{k_B T_K}{\mu_{\text{NH}_3} m_H}}, \quad (3)$$

where μ_{NH_3} is the ammonia molecular weight (equal to 17.03). Assuming that the two quantities are independent, they add in quadrature,

$$\sigma_V^2 = \sigma_{\text{Th}}^2 + \sigma_{\text{NT}}^2 \rightarrow \sigma_{\text{NT}} = \sqrt{\sigma_V^2 - \sigma_{\text{Th}}^2}. \quad (4)$$

σ_{NT} takes into account all gas motions unrelated to thermal effects, such as turbulence. Dense cores are argued to form from large-scale ($> 0.1 \text{ pc}$) turbulence dissipation due to shock compressions (Elmegreen & Scalo 2004; Mac Low & Klessen 2004). It is therefore important to spatially resolve the internal turbulence in the core, and to try to correlate it with the effects of protostellar feedback. We thus compute the σ_{NT}/C_s ratio pixel by pixel, making use of Equation (2) and the kinetic temperature derived from our molecular line fitting and show the results in Figure 10. A large portion of the coherent core is characterized by subsonic motions: the ratio reaches a minimum value of $\sigma_{\text{NT}}/C_s = 0.54 \pm 0.05$, and the mean for pixels with $\log[N(\text{NH}_3)] > 14.4$ is $\langle \sigma_{\text{NT}}/C_s \rangle = 0.80$. It is interesting to note that, within our map coverage, only class II sources are found in the line of sight of subsonic motions, reinforcing the idea that they are off-core objects. On the other hand, younger objects are located on the edge of the transonic transition B09 or B10 or in zones of supersonic motions (B11). The transition between subsonic and supersonic media appears to be sharp, as found by other studies (Foster et al. 2009; Pineda et al. 2010). The maximum value found for the σ_{NT}/C_s ratio is 1.65 ± 0.31 . The enhancement of nonthermal motions in the north is most likely due to the B11 (and possibly B09 and B10) bipolar outflow, which is injecting turbulence in the core as also seen with hydrodynamic simulations (Offner & Arce 2014). In fact, one of the outflow lobes is spatially correlated with the region with the highest σ_{NT}/C_s values (see Figure 8 from Duarte-Cabral et al. 2012).

In order to inspect the correlation between σ_V or σ_{NT}/C_s and the YSO positions, we have produced scatter plots of these two quantities and T_{peak} (the peak temperature in the (1, 1) spectra). An example is shown in Figure 11, which focuses on B11. We have used two different data sets: where available, we have taken points from the original (unsmoothed and unregridged,

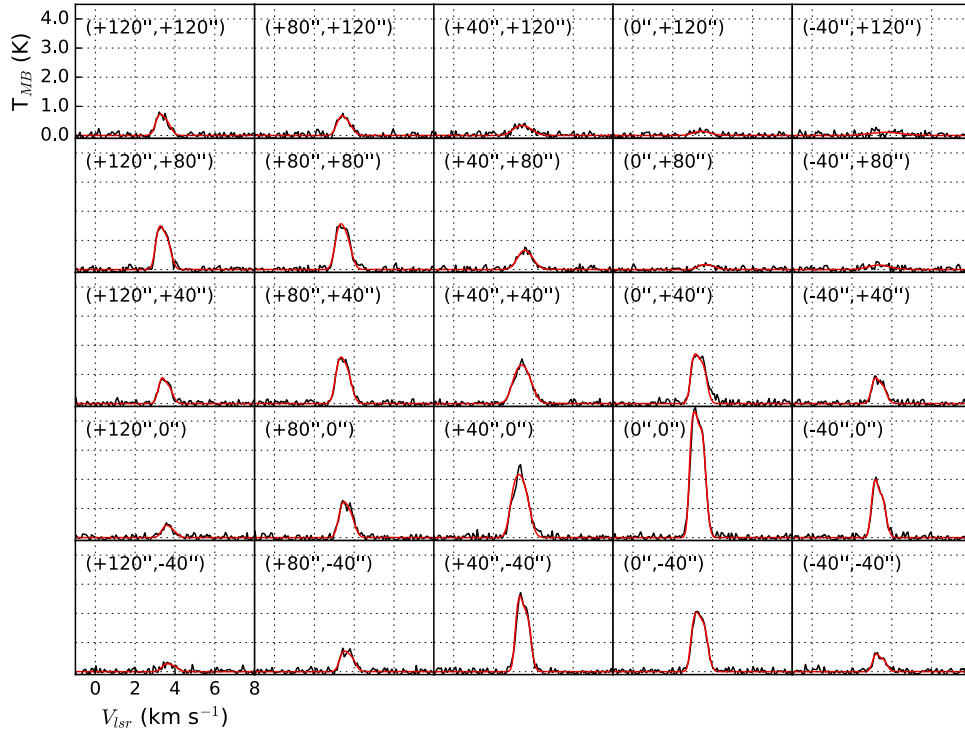


Figure 4. NH_3 (1, 1) observed spectra (black) and best-fit model (red) at 25 different positions. Only the main component is shown. In each panel, the offset from the position R.A. = $17^{\text{h}}11^{\text{m}}19^{\text{s}}.99$, decl. = $-27^{\circ}26'27''.3$ (J2000) is indicated as $(\Delta\text{R.A.}, \Delta\text{decl.})$ in arcsec.

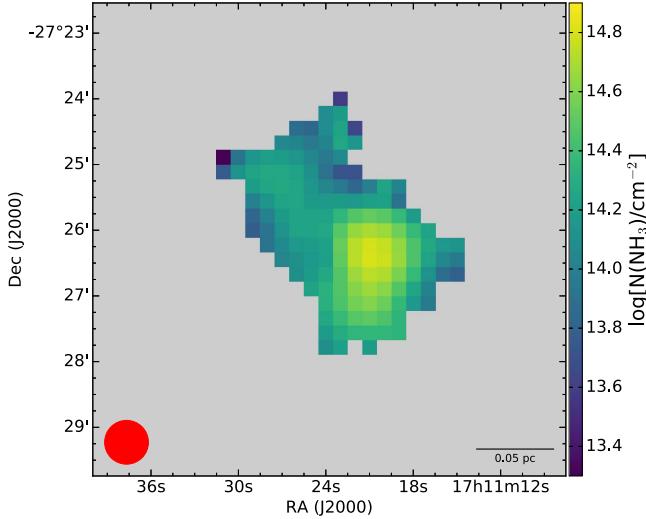


Figure 5. Ammonia column density map obtained in Barnard 59. The median uncertainty obtained is 0.04.

native resolution $=31''.8$) map (green dots), while for the outskirts of the source, where the original S/N is low, we have used the smoothed and regridded maps (violet dots), which have a resolution of $40''$ (see Section 2.2). The red points indicate positions within a smoothed beam size from the YSO B11 (i.e., the distance from the latter is less than $20''$). A general trend is seen: at high T_{peak} (which correlates with the NH_3 column density), the velocity dispersion is often below the sonic speed ($\approx 0.20 \text{ km s}^{-1}$). For $T_{\text{peak}} < 2 \text{ K}$, σ_V values increase, in a similar way as that reported by Pineda et al. (2010). The plot also reveals a trend of the velocity dispersion in the YSO surroundings, as suggested by the fact that red points are mainly located at high velocity dispersions. We have

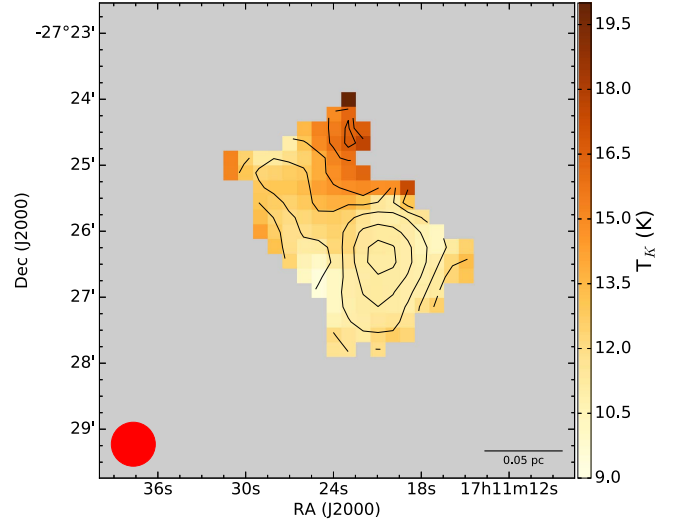


Figure 6. T_K map of the source. The parameter median uncertainty is 0.5 K. Contours show the NH_3 column density $\log[N(\text{NH}_3)/\text{cm}^{-2}]$ at the following levels: [14.0, 14.2, 14.4, 14.6, 14.75].

performed the same analysis on all of the sources covered by our data, computing the mean σ_V and dispersion over a beam size around each one. Results are summarized in Table 3.

We have also studied how the σ_{NT}/C_S ratio correlates with T_{peak} , and Figure 12 shows the respective scatter plot. The quiescent nature of the coherent core is clearly visible at high T_{peak} . Red points, as previously described, indicate pixels closer than $20''$ to B11. We have computed the mean and standard deviation of the ratio in the surroundings of all the available YSOs. Table 3 summarizes these values as well.

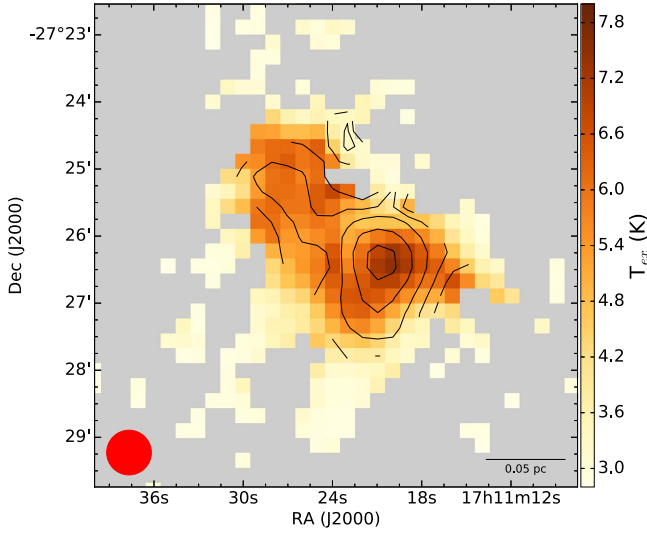


Figure 7. T_{ex} map in B59. The median uncertainty is 0.3 K. The contours are the same as those in Figure 6.

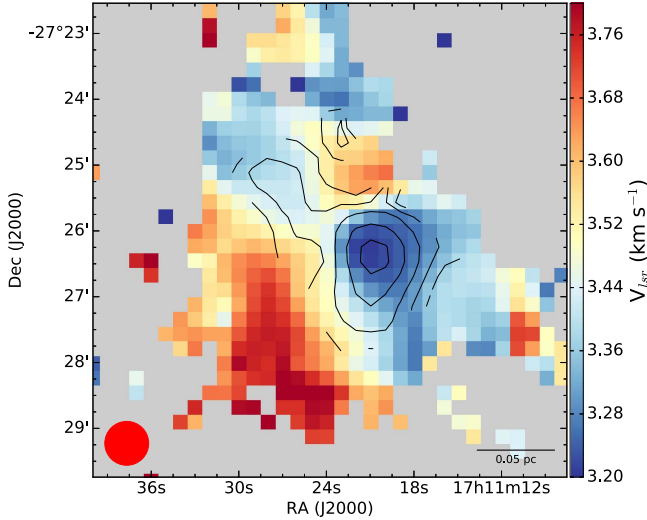


Figure 8. V_{lsr} map in B59. The median uncertainty across the map is 0.03 km s^{-1} . Contours show $N(\text{NH}_3)$ levels as in Figure 6.

Class II objects usually present low mean velocity dispersion values if compared with the sonic speed, and, where available, their mean σ_{NT}/C_s is less than 1.0. There are two exceptions: B03, which is located very close to the edge of our map coverage, and B12, which is too close to B11 to be disentangled with our smoothed angular resolution. Among the younger sources, on the other hand, B09, B10, and B11 are found in a more turbulent environment. B10 and B11, in particular, show the highest values for both the analyzed variables. This can suggest that they are truly embedded in the cloud and that they are affecting through protostellar feedback the surrounding gas.

5. Comparison between H_2 and NH_3

5.1. Column Density and Temperature

NH_3 (1, 1) and (2, 2) transitions are usually a tracer of cold (10–20 K) gas (Ho & Townes 1983), as shown by many observational works (Rosolowsky et al. 2008; Friesen et al. 2009, 2017; Pineda et al. 2015). Using temperature as a

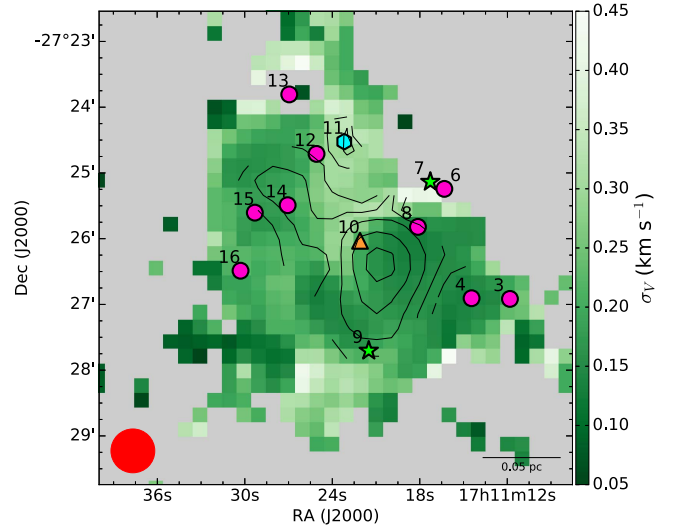


Figure 9. Intrinsic velocity dispersion, σ_v , map of B59 derived from the line fit. The median uncertainty is 0.03 km s^{-1} . Contours show $N(\text{NH}_3)$ levels as in Figure 6. The markers show the YSOs positions labeled following Brooke et al. (2007) classification (cyan hexagon: Class 0/I; orange triangles: Class I; green stars: Class I/II; magenta circles: Class II).

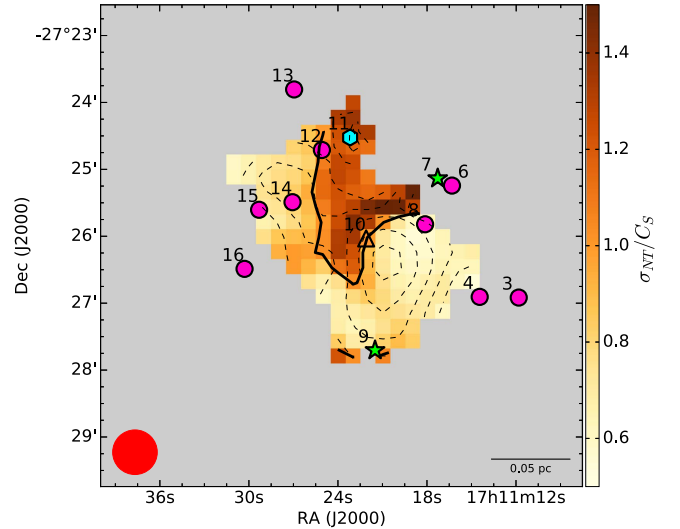


Figure 10. Obtained map of σ_{NT}/C_s , which has a median uncertainty of 0.04. The black line shows the transition from subsonic to supersonic regime ($\sigma_{\text{NT}}/C_s = 1.0$). The YSO positions and the NH_3 column density contours are indicated as in the previous image.

proxy to assess the coupling between molecular gas and dust, we accessed *Herschel* SPIRE data to determine maps of H_2 column density and dust temperature T_{dust} , following the approach described in Appendix B. The SPIRE maps at 250 and $350 \mu\text{m}$ were smoothed to the resolution of the $500 \mu\text{m}$ one, leading to a common angular resolution of $\text{FWHM} = 38''/4$, which is comparable to the resolution of the smoothed GBT data. Furthermore, we performed a simple background subtraction by computing the average flux density in the surrounding of the source ($d \lesssim 12'$) for each wavelength. The 3σ contour ($\approx 0.18 \text{ K km s}^{-1}$) in the (1, 1) integrated intensity map was chosen to set the external edge of the source. After a few tests, this region selection to compute the background contribution appeared to be the best to eliminate the warmer surrounding medium component, which otherwise

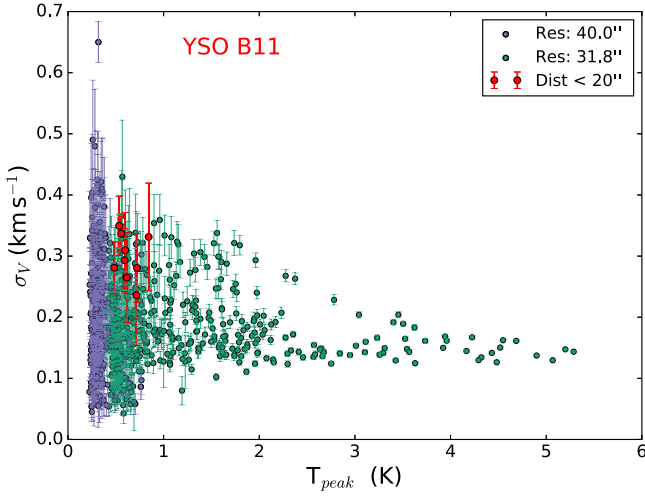


Figure 11. Scatter plot of σ_V as a function of T_{peak} . Points from the original, higher-resolution maps are shown with green dots, while violet ones come from the smoothed and regrided maps and are used when the former are not available. Red dots are positions within a beam size from B11.

Table 3
Results from the Analysis of σ_V and σ_{NT}/C_S Ratio Maps
in Correlation with YSOs Positions

YSO id	IR Spectral Class	σ_V (km s $^{-1}$)	σ_{NT}/C_S
B03	II	0.21 ± 0.06	...
B04	II	0.14 ± 0.01	...
B08	II	0.16 ± 0.05	0.58 ± 0.07
B09	I/II	0.22 ± 0.05	0.84 ± 0.18
B10	I	0.23 ± 0.06	1.06 ± 0.29
B11	0/I	0.30 ± 0.03	1.21 ± 0.08
B12	II	0.26 ± 0.06	0.94 ± 0.17
B14	II	0.19 ± 0.03	0.80 ± 0.12
B15	II	0.17 ± 0.02	0.71 ± 0.06
B16	II	0.18 ± 0.04	...

Note. Missing values represent sources not covered by the T_K Map. The YSO spectral classes from Brooke et al. (2007) are also indicated.

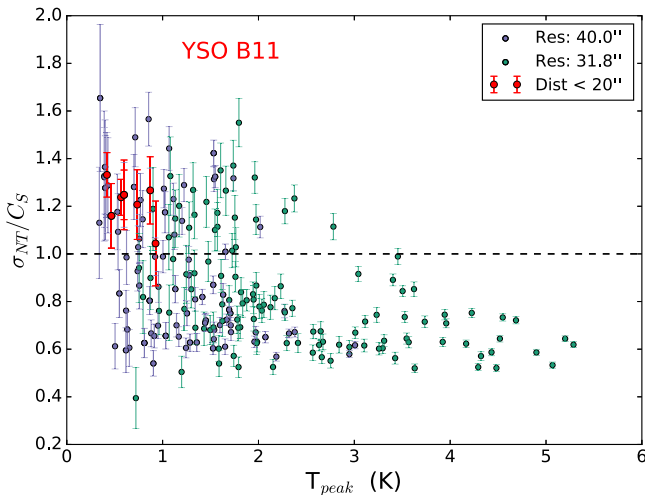


Figure 12. Scatter plot of the ratio between σ_{NT} and C_S vs. T_{peak} . The color code is the same as in Figure 11. The black, dashed line marks the transonic level.

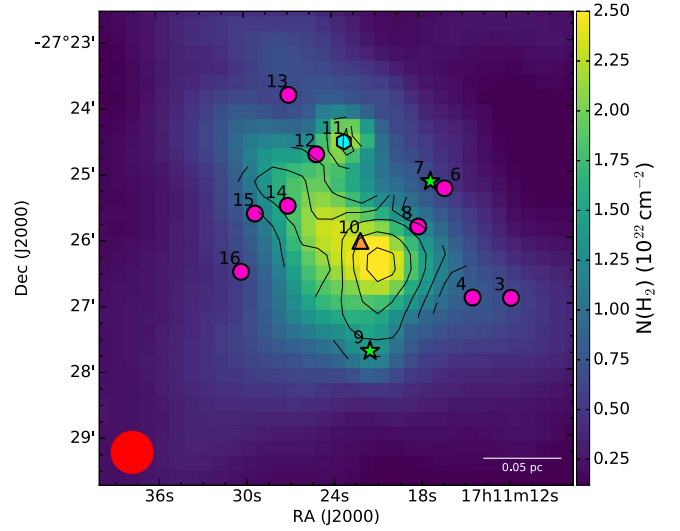


Figure 13. H_2 column density map. The median uncertainty is $0.04 \cdot 10^{22} \text{ cm}^{-2}$. Contours represent $\log[N(\text{NH}_3)]$ as in Figure 6. YSO positions are also indicated, as defined in Figure 9.

would affect the estimation of the column density and dust temperature.²² Finally, the maps were regrided to the same pixel size of the ammonia ones, to allow one-to-one comparisons of the two data sets.

Figure 13 shows the derived $N(\text{H}_2)$ with contours from $N(\text{NH}_3)$. As expected, the two quantities present a similar distribution. The $N(\text{H}_2)$ peak at $\log[N(\text{H}_2)] = (22.43 \pm 0.06)$ is found within a beam size of the $N(\text{NH}_3)$ peak. The average value computed in the coherent core ($\log[N(\text{NH}_3)] > 14.4$) is $\langle \log[N(\text{H}_2)] \rangle = (22.30 \pm 0.09)$. Both maps do not show a clear correlation with the young sources' positions, with the exception of B11, which is visible as an enhancement in both the NH_3 and H_2 data. If we take into account a circular region of $25''$ of radius around that YSO, we find mean values of $\langle \log[N(\text{H}_2)] \rangle = (22.26 \pm 0.07)$ and $\langle \log[N(\text{NH}_3)] \rangle = 14.04$. In the coldest and densest part of the core, this level of H_2 column density corresponds to ammonia values of at least $\log[N(\text{NH}_3)] \approx 14.2$. This difference can suggest that NH_3 is depleted in B11, possibly due to chemical effects. For example, at $T_{\text{dust}} \approx 20$ K, CO molecules, which have previously suffered from freeze-out onto dust grains, start to evaporate and return to the gas phase, destroying the NH_3 precursors (Charnley & Rodgers 2002; Rodgers & Charnley 2008).

The CO evaporation is possibly due to internal heating, as suggested by the T_{dust} map shown in Figure 14. The image shows few warmer condensations in proximity of some YSOs. B11 is the hottest spot, with a peak value of $T_{\text{dust}} = (21.8 \pm 2.2)$ K, and an average (within a beam size) of $\langle T_{\text{dust}} \rangle = (20.6 \pm 1.1)$ K. At this temperature, CO starts to evaporate from dust and impact the ammonia abundance (Tielens 2005). For the surroundings of B06 and B07 (which cannot be disentangled with our spatial resolution), we find $\langle T_{\text{dust}} \rangle = (18.8 \pm 0.7)$ K. Around B13 and B16, we obtain $\langle T_{\text{dust}} \rangle = (16.5 \pm 0.4)$ K and $\langle T_{\text{dust}} \rangle = (16.2 \pm 0.2)$ K, respectively. None of these sources, however, is covered by the NH_3 data with the exception of B11. The mean temperature

²² We also tested a background subtraction approach consisting in a cut of low spatial frequency components in the Fourier space. This gave results consistent to the ones obtained with the method described in the text, within the uncertainties.

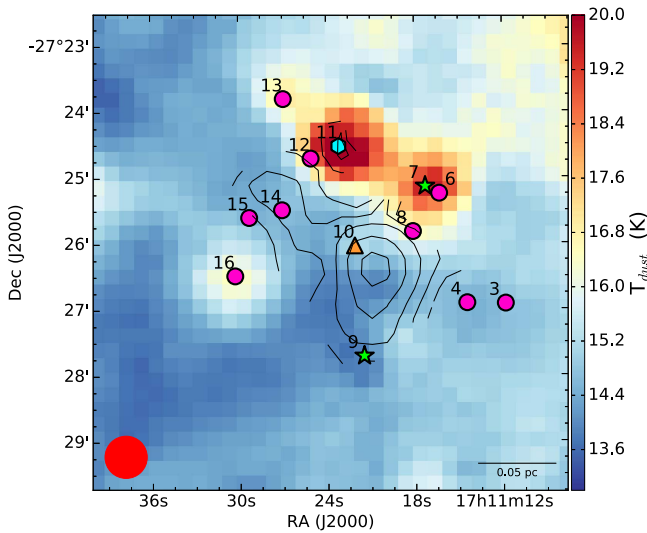


Figure 14. *Herschel* based T_{dust} map with overlaying YSO positions and $N(\text{NH}_3)$ contours, as in the previous figures. The characteristic uncertainty is 0.7 K.

observed for the entire source, using a threshold of $\log[N(\text{H}_2)] > 21.6$, is $\langle T_{\text{dust}} \rangle = (15.2 \pm 1.4)$ K.

Figure 15 shows a scatter plot of T_K and T_{dust} . The dashed curve denotes the line of unity, and it is interesting that almost all points lie below it within errorbars. This difference means that dust temperature overestimates the kinetic one, likely because *Herschel* is more sensitive to more extended, warmer emission than ammonia observations (even after excluding background and foreground emission). As a result, the dust temperature, which is an average along the line of sight, is systematically higher than the kinetic temperature traced by NH_3 , which traces mostly the dense portions of B59. Green dots indicate the coherent core, and they confirm the presence of an almost isothermal structure. Red dots show positions closer than $35''$ around B11 (a circular region that comprehends most of the hot, clumpy feature around the YSO visible in Figure 14), and as expected they present the highest values, supporting the scenario in which this source is actively heating its surroundings, also because T_{dust} decreases away from B11 center in all directions, thus excluding possible enhancements due to the external irradiation from the nearby Sco OB2 association.

5.2. Ammonia Abundance

The canonical way to compute ammonia molecular abundance consists of taking the ratio between its column density and the H_2 column density: $X(\text{NH}_3) = N(\text{NH}_3) / N(\text{H}_2)$. A more robust approach involves the so-called zero-point column density, i.e., the minimum H_2 column density at which NH_3 starts to be detected, indicated as $N(\text{H}_2)_0$ (see Pineda et al. 2008 for a similar approach for CO isotopologues). Therefore, the relation between NH_3 and H_2 column density in linear scale reads

$$N(\text{NH}_3) = X(\text{NH}_3) \cdot N(\text{H}_2) + K, \quad (5)$$

where K is a negative constant related to $N(\text{H}_2)_0$. We perform a linear least squares regression fit to the data to obtain both K and the molecular abundance. For convenience, we inverted Equation (5) and fitted the relation

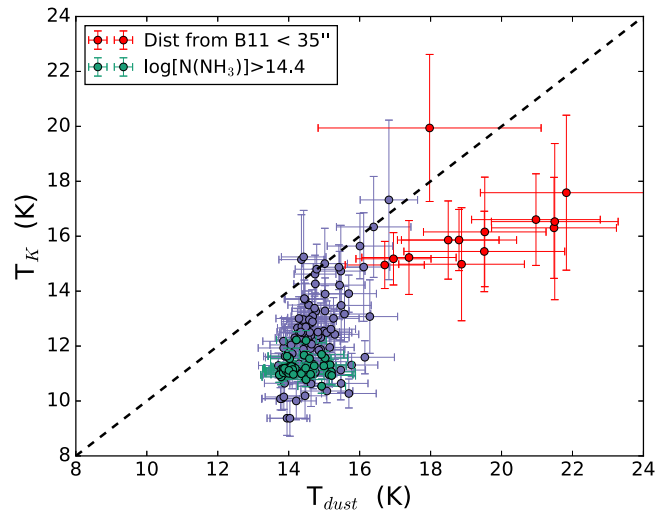


Figure 15. Scatter plot of T_K vs. T_{dust} . The black, dashed line represents the 1:1 relation. Green points indicate the coherent core ($\log[N(\text{NH}_3)] > 14.4$), red ones are closer than $35''$ from B11, and violet dots come from the rest of the source.

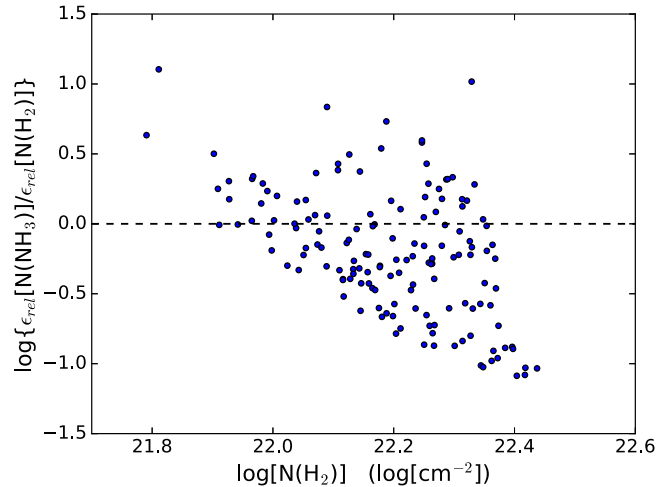


Figure 16. Ratio of the $N(\text{NH}_3)$ relative uncertainties ($\epsilon_{\text{rel}}(\text{NH}_3)/N(\text{NH}_3)$) over the $N(\text{H}_2)$ ones in logarithmic scale, plotted vs. $\log[N(\text{H}_2)]$. The black dashed line indicates where the ratio is equal to 1.0, below which the majority of the points is found.

$N(\text{H}_2) = m \cdot N(\text{NH}_3) + N(\text{H}_2)_0$ (where $m = 1/X(\text{NH}_3)$) to consider only uncertainties on $N(\text{H}_2)$, which are usually larger than those on $N(\text{NH}_3)$. Figure 16 shows the ratio between the relative uncertainties on $N(\text{NH}_3)$ ($\epsilon_{\text{rel}}[N(\text{NH}_3)]$) and the ones on $N(\text{H}_2)$ ($\epsilon_{\text{rel}}[N(\text{H}_2)]$).²³ The results of the linear fit are listed in Table 4.

The zero-point column density found is in agreement with the value of $A_V = 7$ mag used by the GAS survey as a threshold value for detection of NH_3 emission. The $X(\text{NH}_3)$ value we obtain has to be considered an average across the source, and it is in good agreement with other low-mass star-forming regions, such as Ophiuchus ($X(\text{NH}_3) = 1\text{--}10 \cdot 10^{-8}$, Friesen et al. 2009) and Perseus ($X(\text{NH}_3) = 1\text{--}8 \cdot 10^{-8}$, Foster et al. 2009). With the parameters just obtained, we can also

²³ The relative uncertainty ϵ of a quantity ($X \pm \sigma_X$) is computed as $\epsilon[X] = \sigma_X/X$.

Table 4
Best-fit Parameters for $N(\text{H}_2)$ – $N(\text{NH}_3)$ Relation

Parameter	Value
m (10^7)	(3.45 ± 0.26)
$N(\text{H}_2)_0$ (10^{21}cm^{-2})	(6.38 ± 0.38)
$X(\text{NH}_3)$ (10^{-8})	(2.90 ± 0.22)
A_V^a (mag)	(6.79 ± 0.40)
r^b	0.619

Notes.

^a Extinction in magnitude calculated using the relation $N(\text{H}_2) = 9.4 \cdot 10^{20} (A_V/\text{mag}) \text{cm}^{-2}$ (Bohlin et al. 1978).

^b Linear correlation coefficient.

recover the abundance map, computing pixel by pixel:

$$X(\text{NH}_3) = \frac{N(\text{NH}_3)}{N(\text{H}_2) - N(\text{H}_2)_0}. \quad (6)$$

The spatial distribution of $X(\text{NH}_3)$ is shown in Figure 17. Interestingly, the ammonia abundance near the position of B11 is very low compared to the densest coherent core, confirming the NH_3 depletion in this area mentioned in the previous sections.

6. Core Dynamical State

We investigate the core dynamical state by means of the virial ratio, usually defined as $\alpha_{\text{vir}} = M_{\text{vir}}/M$ (Bertoldi & McKee 1992), where M and M_{vir} are the source mass and virial mass, respectively. If we consider only the contribution of the kinetic energy K and the gravitational potential energy U to the source stability, the last equation can be expressed as

$$\alpha_{\text{vir}} = \frac{2K}{|U|}. \quad (7)$$

The kinetic term, which comprises both thermal and turbulent motions, is computed as

$$K = \frac{3}{2} M \sigma_{\text{vir}}^2, \quad (8)$$

where M is the mass and σ_{vir} is the total, one-dimensional velocity dispersion of the gas (the factor 3 takes into account components in the other two spatial directions, assuming an isotropic velocity distribution). σ_{vir} can be derived assuming that the nonthermal component of the overall molecular gas velocity is the same as in the NH_3 one. Then

$$\begin{aligned} \sigma_{\text{vir}}^2 &= \sigma_{\text{tot,NT}}^2 + \sigma_{\text{tot,T}}^2, \\ \sigma_{\text{vir}}^2 &= \sigma_V^2 - \sigma_{\text{NH}_3,T}^2 + \sigma_{\text{tot,T}}^2 = \sigma_V^2 - \frac{k_B T_K}{\mu_{\text{NH}_3} m_H} + \frac{k_B T_K}{\mu m_H}. \end{aligned} \quad (9)$$

The velocity dispersion is computed pixel by pixel, and the mean value over the obtained map is $\sigma_{\text{vir}} = (0.29 \pm 0.05) \text{ km s}^{-1}$.

Figure 18 shows the $870 \mu\text{m}$ continuum image of B59 from APEX. The source mass has been calculated using these

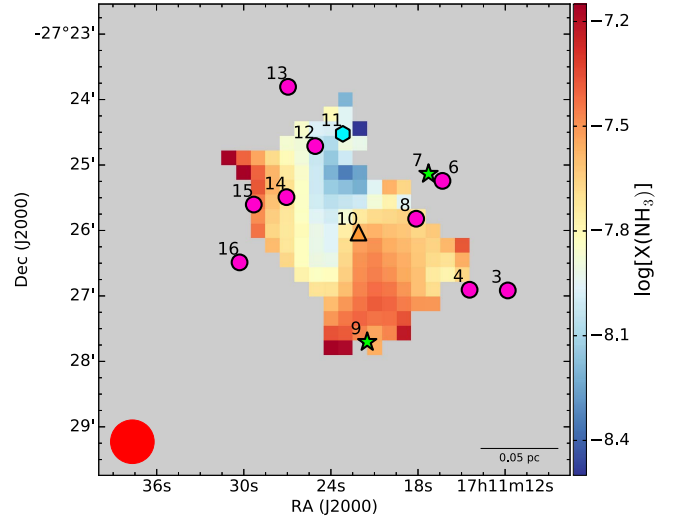


Figure 17. $X(\text{NH}_3)$ map obtained with the approach described in the text. The median uncertainty is $0.3 \cdot 10^{-8}$. YSO positions are also indicated.

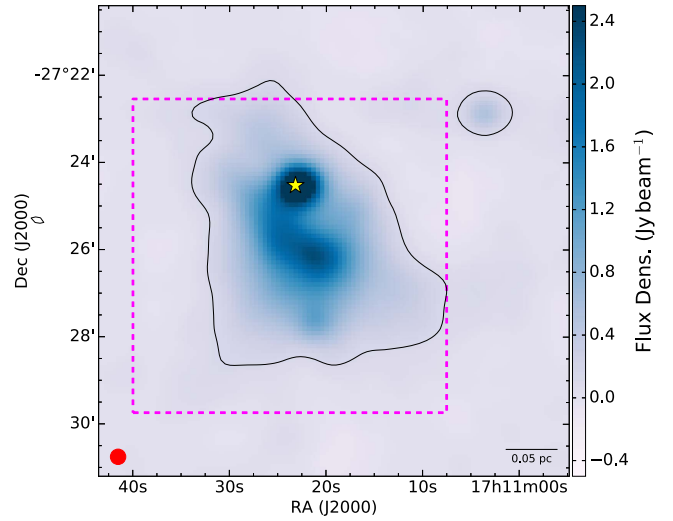


Figure 18. APEX map showing thermal dust emission at $870 \mu\text{m}$. The contour shows the 5σ level used in the mass computation ($\sigma = 0.026 \text{ Jy/beam}$). The bright region in the top-right corner, corresponding to the position of the YSO BHB07-01 (B01), was excluded from the virial analysis. The yellow star shows the position of B11, and the magenta box shows the extension of ammonia data.

emission data at $870 \mu\text{m}$ and

$$M = f \frac{D^2 S_\nu}{B_\nu(T_{\text{dust}}) \kappa_\nu}, \quad (10)$$

where f is the gas-to-dust ratio, assumed to be 100 (Hildebrand 1983), $D = (145 \pm 16) \text{ pc}$ is the source distance (Alves & Franco 2007), and $B_\nu(T_{\text{dust}})$ is the Planck function at a given dust temperature, which is assumed to be $T_{\text{dust}} = 15 \text{ K}$ (consistent with the mean value found in the T_{dust} map, see Section 5.1). To be consistent with the *Herschel* data analysis (see Section 5), we have calculated the opacity at $870 \mu\text{m}$ following

$$\kappa_{870} = \kappa_{250} \left(\frac{250 \mu\text{m}}{870 \mu\text{m}} \right)^\beta = 1.54 \text{ cm}^2 \text{ g}^{-1}, \quad (11)$$

where the reference value at $250 \mu\text{m}$ is $\kappa_{250} = 10.0 \text{ cm}^2 \text{ g}^{-1}$ (Hildebrand 1983) and $\beta = 1.5$. S_ν is the total flux at $870 \mu\text{m}$ derived from the 5σ contour of the APEX map. In Figure 18, the bright envelope of B11 is clearly visible. Since we are interested in the cold core for the virial analysis, we fitted a bi-dimensional Gaussian to the source to derive its integrated intensity flux. The calculation gives $S_{\text{B11}} = 15 \text{ Jy}$, and we subtracted this value to the total flux S_ν . The uncertainty on the latter has been estimated taking into account the calibration uncertainty (10%, Dumke & Mac-Auliffe 2010). The computed total flux is $(111 \pm 11) \text{ Jy}$ and the obtained mass is $M = (24.2 \pm 5.9) M_\odot$. This value is in good agreement with previous estimations (Rathborne et al. 2009; Román-Zúñiga et al. 2009; Duarte-Cabral et al. 2012). It is worth saying that if we apply the same approach to compute the mass from the *Herschel* fluxes, we obtain a result of $M \approx 10 M_\odot$, a factor of 2 lower than our estimation with APEX. This difference can be due to multiple reasons, such as the dust opacity intrinsic uncertainty or possibly too harsh background subtraction on the *Herschel* maps (which is though to be necessary to compare the ammonia results with the dust emission arising for the very same region). Moreover, at SPIRE wavelengths, the Planck function is more sensible to the temperature than at APEX one. Given all of these, the discrepancy found seems reasonable, and the following analysis will be done with the APEX derived results.

The gravitational energy has been computed considering the source as a sphere, with a density distribution of the form $\rho \propto r^{-k}$:

$$U = -a \frac{3}{5} \frac{GM^2}{R}, \quad (12)$$

where $a = (1 - k/3)/(1 - 2k/5)$, and we have set $k = 1.0$, a value that we later let vary. The radius R corresponds to the effective radius of a circle with the same area of the region used to compute the total flux. We obtain $R = (0.120 \pm 0.013) \text{ pc}$. The result for the virial ratio is then $\alpha_{\text{vir}} = (0.43 \pm 0.19)$, where the uncertainty has been calculated using standard error propagation. The B59 core is thus gravitationally virialized. The value of the virial parameter that we obtain is indeed low compared to values found in others studies of low-mass star-forming regions, according to which most of the cores are pressure confined (see, for instance, Pattle et al. 2015 or Kirk et al. 2017). This confinement situation is also true in the Pipe, where the core population is mainly pressure confined, as shown by Lada et al. (2008). As in other similar studies (i.e., Kauffmann et al. 2013), these authors also indicated a trend between the virial parameter and the core mass: the higher the mass, the lower α_{vir} . If we extrapolate their relation $\alpha_{\text{vir}} \propto M^{-0.66}$ at a mass of $25 M_\odot$ (approximately the mass of B59), we obtain $\alpha_{\text{vir}} \approx 0.80$, not far from the results in our analysis, once errors are taken into account.

Our results are robust against variations in the assumptions made for the various parameters. The dust spectral index β , for example, is usually taken in the range of $[1.5, 2.0]$ in star-forming regions at core scales. An increment in its value corresponds to an increment in the computed dust mass, making the core even more sub-virial (for instance, $\beta = 1.7$

leads to $\alpha_{\text{vir}} = 0.33$). The other parameter for which we make a strong assumption is the slope k of the density profile, which can vary from $k = 0$ ($a = 1$, flat profile) to $k = 2.5$ (then $a \rightarrow \infty$). Taking as extremal cases $k = 0$ and $k = 2.0$, the virial parameter values obtained are $\alpha_{\text{vir}} = 0.47$ and $\alpha_{\text{vir}} = 0.28$ respectively. Within these variations of the parameters, thus, the core is still gravitationally bound.

The virial analysis just described assumes that B59 is a single core. This assumption is supported by the investigation of Román-Zúñiga et al. (2012), who computed an extinction map across the source carefully subtracting the YSOs' contribution. The resulting profile is monolithic, leading to the conclusion that B59 is not fragmented in multiple cores, and it should collapse as a whole structure. Nevertheless, to our knowledge, in the literature there has not been any detection of contraction of the core. Ammonia inversion transitions are not suitable to detect infall asymmetries, due to their low critical density and opacity. However, contraction motions within dense cores also produce line broadening at their very center (see, e.g., Caselli et al. 2002), and our ammonia spectra do not exhibit any sign of this broadening. If the core is not collapsing, a mechanism of support against gravity is needed, and it can possibly be found in the magnetic field. We can estimate the magnetic field strength B needed to balance the gravitational pressure by including the magnetic energy term in the virial theorem:

$$U + 2T + \Omega_B + \Omega_P = 0, \quad (13)$$

where $\Omega_B = V \cdot B^2/(2\mu_0)$, where V is the source volume (assuming spherical geometry: $V = 4\pi R^3/3$) and μ_0 is the vacuum permeability. Here Ω_P is the external pressure term, which takes into account the confining pressure arising from the cloud weight (P_w) and the turbulence pressure exerted by the higher velocity dispersion and lower density medium that surrounds the core (P_t). Using the formalism introduced by Pattle et al. (2015), one has $\Omega_P = -4\pi R^3(P_w + P_t)$. The turbulent term can be expressed as $P_t = \rho_t \sigma_t^2$, where ρ_t and σ_t are, respectively, the density and the velocity dispersion of the turbulent surrounding medium. The pressure due to the cloud weight, on the other hand, is $P_w = \pi G \Sigma \Sigma_s (\mu m_H)^2$, where Σ is the mean column density of the cloud and Σ_s the column density at the source position (see Appendix A in Kirk et al. 2017). For the present work, we use the estimations for the two pressures made by Lada et al. (2008), according to which $P_w = 1.38 \cdot 10^{-12} \text{ Pa}$ and $P_t = 6.90 \cdot 10^{-13} \text{ Pa}$. Inverting Equation (13), and using the expressions for U and T previously introduced, we obtain

$$B = \sqrt{\frac{3\mu_0}{2\pi R^3} (|U| + |\Omega_P| - 2T)} = (140 \pm 65) \mu\text{G}, \quad (14)$$

which has to be considered a lower limit, since it represents the minimum B strength able to halt the gravitational contraction. The magnetic field strength of the Pipe Nebula at the cloud scale (i.e., at a volume density $n \approx 10^3 \text{ cm}^{-3}$) toward B59 is $\approx 17 \mu\text{G}$ (Alves et al. 2008). Given the peak H_2 column density and the source radius that we have derived in the spherical approach, we can estimate that our data are tracing a medium with an average volume density of $\approx 4 \cdot 10^4 \text{ cm}^{-3}$. Crutcher (1999) estimated that if the magnetic field is unimportant in the collapse, $B \propto \rho^{2/3}$ while if it is dominant over gravity

$B \propto \rho^{1/2}$. Scaling the value found in Alves et al. (2008) to our density with these two models, we obtain $B \approx 200 \mu\text{G}$ and $B \approx 110 \mu\text{G}$, respectively, in good agreement with our estimations. Given the uncertainties, we thus cannot discriminate between the two scenarios discussed by Crutcher (1999).

7. Conclusions

We have investigated the protostellar core B59 using primarily ammonia inversion transition spectra and ancillary dust continuum data, achieving a comprehensive view of the kinematics and dynamics of the core. The spectral fit performed on NH_3 spectra reveals that B59 has a prominent cold, dense, and velocity-coherent structure. The analysis of the turbulence level in the region shows that the nonthermal motions at the coherent core are subsonic, with a sharp transition to a supersonic regime in the surroundings. The coherent core is not clearly associated with any YSO identified in the c2d survey. In the northern part of the source, in correspondence with the position of B11, there is a change in the dynamical scenario, with higher velocity dispersion and temperature with respect to the quiescent and cold core. Here the kinetic temperatures are as high as 16–18 K, possibly requiring an extra source of heating in addition to the standard radiation field. This heating is most likely due to the internal radiation of B11, which is supported by the high levels of dust thermal emission from its dense envelope. B11 also powers a bipolar outflow likely responsible for the supersonic gas motions seen with the molecular data. The YSO envelope is deficient in ammonia, most likely due to depletion produced by the release of CO from dust grains back to the gas phase.

We have analyzed the velocity dispersion map and σ_{NT}/C_S ratio to study the core kinematics. Sources B10 and B11 are associated with supersonic turbulent motions, suggesting that they are truly embedded within the source and are affecting through outflow feedback the surrounding gas. On the contrary, sources B04, B08, B14, B15, and B16 (which are all Class II objects) are found in quiescent regions, where the gas is subsonic. Most likely, these are foreground or background objects with respect to the material traced by ammonia. B03 and B09 presents σ_V values close to the transonic limit, while the σ_{NT}/C_S value (available only for the latter) is consistent with subsonic turbulent motions. Since these two YSOs are found close to the edge of our map's coverage, we do not draw any conclusion about them. In the case of B12 as well our analysis is not conclusive, since with our smoothed angular resolution this source is within one beam of distance from B11.

The virial ratio obtained analyzing the dust emission is well below its critical value, indicating that the core is sub-virial and gravitationally bounded. This result suggests that the protostellar feedback affects the source only locally, and does not impact its global dynamics. Given such a low virial parameter, and since the extinction map of the core exhibits a monolithic profile (Román-Zúñiga et al. 2012), Barnard 59 should be collapsing as a whole structure. Nevertheless, no signs of such a contraction are known to the present day. Our ammonia data do not show a line broadening at the center of the core, which is usually an indication of contracting motions. Further investigations of the source with other molecular tracers, more suitable for the detection of infall asymmetries (such as HCO^+ and isotopologues) will possibly confirm this hypothesis. Moreover, higher resolution VLA data will help us resolve possible

substructures within the source, testing the hypothesis that Barnard 59 is a monolithic structure.

If the core is truly in equilibrium, since, in our virial analysis, we have taken into account only the internal pressure given by thermal and turbulent motions, the aforementioned considerations lead to the conclusion that another source of pressure is halting the gravitational collapse. Most likely, this source of support has to be the magnetic field, for which we have estimated a lower limit of $B \approx 140 \mu\text{G}$ (see Section 6). At the cloud scale, the Pipe Nebula is characterized by a strong magnetic field (Alves et al. 2008). Future polarization observations of B59 will allow for an estimation of the magnetic pressure term and its role in the dynamical evolution of the core. Nevertheless, our data support the idea that Barnard 59 is not collapsing, and will not form new stars, at least in the near future.

We thank Dr. Jorma Harju for his kind help in the analysis of Herschel data.

Appendix A Determination of Physical Properties from the NH_3 Spectral Fit

The main assumption typically made in NH_3 line analysis is that T_{ex} is the same for all of them (Ho & Townes 1983; Rosolowsky et al. 2008; Friesen et al. 2009). The system is thus characterized by three distinct temperatures:

1. kinetic temperature T_K , which establishes the Maxwellian velocity distribution of the gas components;
2. excitation temperature T_{ex} , which regulates the population of upper (u) and lower (l) state in each (J, K) rotational level following a Boltzmann distribution; and
3. rotational temperature T_{rot} , according to which the different rotational levels are populated. Note that the terminology is not fully appropriate, since we are not analyzing purely rotational transitions.

The approach consists of generating a model spectrum in the main beam temperature and performing a nonlinear regression to estimate best-fit parameter values and their uncertainties. The standard solution of the radiative transfer problem asserts that the T_{MB} of a transition is

$$T_{\text{MB}} = A[1 - \exp(-\tau(\nu))], \quad (15)$$

where the amplitude $A = \eta_f(J_\nu(T_{\text{ex}}) - J_\nu(T_b))$. T_b is the background temperature, η_f is the beam filling factor, and $J_\nu(T) = (h\nu/k)(\exp(h\nu/kT) - 1)^{-1}$. Therefore, we express the optical depth $\tau(\nu)$ as a function of the input parameters, i.e., T_{ex} , T_K , V_{lsr} , σ_V , and $N(\text{NH}_3)$. The absorption coefficient per unit of frequency can be written as

$$\alpha_\nu = \frac{c^2}{8\pi\nu_{\text{rest}}^2} \frac{g_u}{g_l} n_l A_{ul} \left[1 - \exp\left(-\frac{\Delta E}{k_B T_{\text{ex}}}\right) \right] \phi(\nu), \quad (16)$$

where $\phi(\nu)$ is the line profile function, which must be normalized to 1. Also, ν_{rest} is the line rest frequency and g_u and g_l are the statistical weights for the upper and lower levels, respectively, and the levels are separated in energy by ΔE . In addition, A_{ul} is the Einstein coefficient and n_l is the lower state density. The latter is related to its upper counterpart n_u through

the Boltzmann equation:

$$\frac{n_u}{n_l} = \frac{N_u}{N_l} = \frac{g_u}{g_l} \exp\left(-\frac{\Delta E}{k_B T_{\text{ex}}}\right). \quad (17)$$

One must note that the first equivalence in (17) holds because we are assuming a homogeneous slab of material, and therefore volume density ratios are equal to column density ones. For the (1, 1) rotational state, $N_{11} = N_u + N_l$. Thus one can easily obtain

$$N_l = \frac{N_{11}}{1 + \frac{g_u}{g_l} \exp\left(-\frac{\Delta E}{k_B T_{\text{ex}}}\right)}. \quad (18)$$

N_{11} is related to N_{22} again according to the Boltzmann equation:

$$\frac{n_{22}}{n_{11}} = \frac{N_{22}}{N_{11}} = \frac{g_{22}}{g_{11}} \exp\left(-\frac{\Delta E_{12}}{k_B T_{\text{rot}}}\right), \quad (19)$$

assuming that ΔE_{12} is the energy difference between the two levels. The total optical depth τ is obtained integrating α_ν over frequency and line of sight:

$$\begin{aligned} \tau &= \iint \alpha_\nu d\nu ds = \frac{c^2}{8\pi\nu_{\text{rest}}^2} \frac{g_u}{g_l} N_l A_{ul} \left[1 - \exp\left(-\frac{\Delta E}{k_B T_{\text{ex}}}\right) \right] \\ &= \frac{c^2}{8\pi\nu_{\text{rest}}^2} \frac{g_u}{g_l} N_{11} A_{ul} \frac{1 - \exp\left(-\frac{\Delta E}{k_B T_{\text{ex}}}\right)}{1 + \frac{g_u}{g_l} \exp\left(-\frac{\Delta E}{k_B T_{\text{ex}}}\right)}. \end{aligned} \quad (20)$$

The Einstein coefficient for dipole emission depends on the dipole matrix element μ_{ul} (Mangum & Shirley 2015):

$$A_{ul} = \frac{64\pi^4 \nu_{\text{rest}}^3}{3hc g_u} |\mu_{ul}|^2. \quad (21)$$

To finally relate T_{MB} and the total column density of the molecule, one can notice that N_{11} is linked to $N(\text{NH}_3)$ through the rotational partition function Z_{rot} :

$$N_{11} = N(\text{NH}_3) \frac{Z_{11}}{Z_{\text{rot}}} = \quad (22)$$

$$\begin{aligned} N(\text{NH}_3) Z_{11} &\left\{ \sum_J (2J+1) \exp \right. \\ &\times \left. \left(-\frac{h[BJ(J+1) + (C-B)J^2]}{k_B T_{\text{rot}}} \right) \right\}^{-1}, \end{aligned} \quad (23)$$

where B and C are the rotational constants, equal to 298,117 and 186,726 MHz (Pickett et al. 1998). We have considered para-states only. To obtain a complete model spectrum, we have to specify the line profile $\phi(\nu)$, which according to our hypothesis is a weighted sum of Gaussian lines, one for each hyperfine component. The weights correspond to the relative intensities and are derived from quantum mechanics calculations (see Mangum & Shirley 2015).

The observed spectra can be fitted using the models produced with the above technique. A further clarification, however, is required: this approach only involves the rotational temperature, while we are mainly interested in the kinetic one.

To obtain the latter, one can consider a three-state system composed of (1, 1), (2, 2), and (2, 1) levels. The transition between different K-ladders is allowed only through collisions. Once the level (2, 1) is populated, it rapidly decays radiatively to the (1, 1). Thus, solving for the detailed balance taking into account spontaneous emission and collisional rates leads to the following equation (Swift et al. 2005):

$$T_{\text{rot}} = T_K \left\{ 1 + \frac{T_K}{T_{12}} \ln [1 + 0.6 \exp(-15.7\text{K}/T_K)] \right\}^{-1}, \quad (24)$$

where T_{12} is the temperature corresponding to ΔE_{12} ($=41.5$ K).

Appendix B Herschel Data Analysis

The dust emission can be modeled as gray-body emission, characterized by a frequency dependent optical depth τ_ν :

$$I_\nu = B_\nu(T)(1 - e^{-\tau_\nu}). \quad (25)$$

The optical depth itself depends on two fundamental quantities: the opacity κ_ν and the mass density ρ of the source:

$$\tau_\nu = \int_{\text{LOS}} \kappa_\nu \rho ds. \quad (26)$$

Given that the gas column density $N(\text{H}_2)$ is the integration of the volume density $n(\text{H}_2)$ along the line of sight, and that $n(\text{H}_2) = \rho/(\mu_{\text{H}_2} m_{\text{H}})$ (where $\mu_{\text{H}_2} = 2.8$ is the mean molecular weight per hydrogen molecule), one obtains

$$N(\text{H}_2) = \frac{\tau_\nu}{\mu_{\text{H}_2} m_{\text{H}} \kappa_\nu}. \quad (27)$$

Therefore, once the optical depth is known, one can infer the column density of the source, assuming that the opacity is known as well. For the latter, a power-law expression is usually adopted, making use of the dust opacity index β :





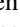



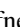





$$\kappa_\nu = \kappa_0 \left(\frac{\nu}{\nu_0} \right)^\beta. \quad (28)$$

We used $\beta_\nu = 1.5$, which seems suitable for star-forming regions (Mezger et al. 1990; Walker et al. 1990) and the dust opacity $\kappa_0 = 0.1 \text{ cm}^2 \text{ g}^{-1}$ (Hildebrand 1983; Beckwith et al. 1990) at the reference frequency corresponding to the wavelength $\lambda_0 = 250 \mu\text{m}$. This value already includes a dust-to-mass ratio of 100. We also took into account the optically thin limit of Equation (25), which reads $I_\nu \approx B_\nu(T) \tau_\nu$.

We fit²⁴ the three photometric points from SPIRE data, taking into account the color corrections for gray-body and extended sources, and we obtain a map of T_{dust} and optical depth. The latter is converted into a column density map according to Equation (27). Uncertainties are evaluated through a Monte Carlo method, iterating the described procedure 1000 times. At each iteration, a random noise is added to the SPIRE maps, taking into account both calibration uncertainties (7%) and the fluctuations that the detector response can present. See SPIRE HandBook (Version 3.1) for details about color corrections or flux uncertainties.

²⁴ See Hardegree-Ullman et al. (2013) for details on the code.

ORCID iDs

E. Redaelli  <https://orcid.org/0000-0002-0528-8125>
 F. O. Alves  <https://orcid.org/0000-0002-7945-064X>
 P. Caselli  <https://orcid.org/0000-0003-1481-7911>
 J. E. Pineda  <https://orcid.org/0000-0002-3972-1978>
 R. K. Friesen  <https://orcid.org/0000-0001-7594-8128>
 C. D. Matzner  <https://orcid.org/0000-0001-9732-2281>
 A. Ginsburg  <https://orcid.org/0000-0001-6431-9633>
 E. Rosolowsky  <https://orcid.org/0000-0002-5204-2259>
 J. Keown  <https://orcid.org/0000-0003-2628-0250>
 S. S. R. Offner  <https://orcid.org/0000-0003-1252-9916>
 J. Di Francesco  <https://orcid.org/0000-0002-9289-2450>
 H. Kirk  <https://orcid.org/0000-0002-5779-8549>
 P. C. Myers  <https://orcid.org/0000-0002-2885-1806>
 A. Cimatti  <https://orcid.org/0000-0002-4409-5633>

References

- Alves, F. O., & Franco, G. A. P. 2007, *A&A*, **470**, 597
 Alves, F. O., Franco, G. A. P., & Girart, J. M. 2008, *A&A*, **486**, L13
 André, P., Men'shchikov, A., Bontemps, S., et al. 2010, *A&A*, **518**, L102
 Andre, P., Ward-Thompson, D., & Barsony, M. 2000, in *Protostars and Planets IV*, ed. V. Mannings, A. P. Boss, & S. S. Russell (Tucson, AZ: Univ. Arizona Press), 59
 Beckwith, S. V. W., Sargent, A. I., Chini, R. S., & Guesten, R. 1990, *AJ*, **99**, 924
 Benson, P. J., & Myers, P. C. 1989, *ApJS*, **71**, 89
 Bertoldi, F., & McKee, C. F. 1992, *ApJ*, **395**, 140
 Bohlin, R. C., Savage, B. D., & Drake, J. F. 1978, *ApJ*, **224**, 132
 Brooke, T. Y., Huard, T. L., Bourke, T. L., et al. 2007, *ApJ*, **655**, 364
 Caselli, P., Benson, P. J., Myers, P. C., & Tafalla, M. 2002, *ApJ*, **572**, 238
 Charnley, S. B., & Rodgers, S. D. 2002, *ApJL*, **569**, L133
 Crutcher, R. M. 1999, *ApJ*, **520**, 706
 Duarte-Cabral, A., Chrysostomou, A., Peretto, N., et al. 2012, *A&A*, **543**, A140
 Dumke, M., & Mac-Auliffe, F. 2010, *Proc. SPIE*, **7737**, 77371J
 Elmegreen, B. G., & Scalo, J. 2004, *ARA&A*, **42**, 211
 Evans, N. J., II, Dunham, M. M., Jørgensen, J. K., et al. 2009, *ApJS*, **181**, 321
 Evans, N. J., II, Rawlings, J. M. C., Shirley, Y. L., & Mundy, L. G. 2001, *ApJ*, **557**, 193
 Forbrich, J., Lada, C. J., Muench, A. A., Alves, J., & Lombardi, M. 2009, *ApJ*, **704**, 292
 Foster, J. B., Rosolowsky, E. W., Kauffmann, J., et al. 2009, *ApJ*, **696**, 298
 Franco, G. A. P., Alves, F. O., & Girart, J. M. 2010, *ApJ*, **723**, 146
 Friesen, R. K., Di Francesco, J., Shirley, Y. L., & Myers, P. C. 2009, *ApJ*, **697**, 1457
 Friesen, R. K., Pineda, J. E., co-PIs, et al. 2017, *ApJ*, **843**, 63
 Ginsburg, A., & Mirocha, J. 2011, PySpecKit: Python Spectroscopic Toolkit, Astrophysics Source Code Library, ascl:1109.001
 Goodman, A. A., Barranco, J. A., Wilner, D. J., & Heyer, M. H. 1998, *ApJ*, **504**, 223
 Hara, C., Shimajiri, Y., Tsukagoshi, T., et al. 2013, *ApJ*, **771**, 128
 Hardegree-Ullman, E., Harju, J., Juvela, M., et al. 2013, *ApJ*, **763**, 45
 Hildebrand, R. H. 1983, *QJRAS*, **24**, 267
 Ho, P. T. P., & Townes, C. H. 1983, *ARA&A*, **21**, 239
 Kauffmann, J., Pillai, T., & Goldsmith, P. F. 2013, *ApJ*, **779**, 185
 Kirk, H., Friesen, R. K., Pineda, J. E., et al. 2017, *ApJ*, **846**, 144
 Lada, C. J., Muench, A. A., Rathborne, J., Alves, J. F., & Lombardi, M. 2008, *ApJ*, **672**, 410
 Lada, C. J., & Wilking, B. A. 1984, *ApJ*, **287**, 610
 Lombardi, M., Alves, J., & Lada, C. J. 2006, *A&A*, **454**, 781
 Mac Low, M.-M., & Klessen, R. S. 2004, *RvMP*, **76**, 125
 Mangum, J. G., Emerson, D. T., & Greisen, E. W. 2007, *A&A*, **474**, 679
 Mangum, J. G., & Shirley, Y. L. 2015, *PASP*, **127**, 266
 Masters, J., Garwood, B., Langston, G., & Shelton, A. 2011, *adass XX*, **442**, 127
 Mezger, P. G., Zylka, R., & Wink, J. E. 1990, *A&A*, **228**, 95
 Myers, P. C., Ladd, E. F., & Fuller, G. A. 1991, *ApJL*, **372**, L95
 Nakamura, F., & Li, Z.-Y. 2008, *ApJ*, **687**, 354
 Offner, S. S. R., & Arce, H. G. 2014, *ApJ*, **784**, 61
 Onishi, T., Kawamura, A., Abe, R., et al. 1999, *PASJ*, **51**, 871
 Palmeirim, P., André, P., Kirk, J., et al. 2013, *A&A*, **550**, A38
 Pattle, K., Ward-Thompson, D., Kirk, J. M., et al. 2015, *MNRAS*, **450**, 1094
 Peretto, N., André, P., Könyves, V., et al. 2012, *A&A*, **541**, A63
 Pickett, H. M., Poynter, R. L., Cohen, E. A., et al. 1998, *JQSRT*, **60**, 883
 Pineda, J. E., Caselli, P., & Goodman, A. A. 2008, *ApJ*, **679**, 481
 Pineda, J. E., Goodman, A. A., Arce, H. G., et al. 2010, *ApJL*, **712**, L116
 Pineda, J. E., Offner, S. S. R., Parker, R. J., et al. 2015, *Natur*, **518**, 213
 Planck Collaboration, Ade, P. A. R., Aghanim, N., et al. 2016, *A&A*, **586**, A138
 Rathborne, J. M., Lada, C. J., Muench, A. A., et al. 2009, *ApJ*, **699**, 742
 Rodgers, S. D., & Charnley, S. B. 2008, *ApJ*, **689**, 1448
 Román-Zúñiga, C. G., Frau, P., Girart, J. M., & Alves, J. F. 2012, *ApJ*, **747**, 149
 Román-Zúñiga, C. G., Lada, C. J., & Alves, J. F. 2009, *ApJ*, **704**, 183
 Rosolowsky, E. W., Pineda, J. E., Foster, J. B., et al. 2008, *ApJS*, **175**, 509
 Seifried, D., & Walch, S. 2015, *MNRAS*, **452**, 2410
 Shirley, Y. L. 2015, *PASP*, **127**, 299
 Swift, J. J., Welch, W. J., & Di Francesco, J. 2005, *ApJ*, **620**, 823
 Tafalla, M., Myers, P. C., Caselli, P., Walmsley, C. M., & Comito, C. 2002, *ApJ*, **569**, 815
 Tielens, A. G. G. M. (ed.) 2005, *The Physics and Chemistry of the Interstellar Medium* (Cambridge: Cambridge Univ. Press)
 Walker, C. K., Adams, F. C., & Lada, C. J. 1990, *ApJ*, **349**, 515
 Zucconi, A., Walmsley, C. M., & Galli, D. 2001, *A&A*, **376**, 650